Uncertainty in identifying contact stiffness in a dovetail attachment for turbine blades

Mechanical Systems and Signal Processing 197 (2023) 110379

Contents lists available at ScienceDirect

Mechanical Systems and Signal Processing

journal homepage: www.elsevier.com/locate/ymssp

Uncertainty in identifying contact stiffness in a dovetail attachment for turbine blades

Daniele Botto *, Matteo Glorioso, Serena Occhipinti, Federica Cuccovillo

Department of Mechanical and Aerospace Engineering - Politecnico di Torino, 10129 Torino, Italy

ARTICLE INFO

Communicated by M.M. Neves

Keywords:
Contact stiffness
Contact model
Blade attachment
Turbine blade

ABSTRACT

Designing bladed disks in turbo engines requires accurate dynamic models to correctly estimate resonance frequencies and related stresses. The contact parameters – stiffness and damping in the blade attachments – are currently among the most significant uncertainties of such models. Dry friction and alternating relative motions between the contact interfaces determine the transition between stick and slip that causes the nonlinear behavior of attachments. Commercial and in-house finite element software make use of specific contact elements to simulate dry friction and the resulting nonlinear behavior. These elements require the friction coefficient as input while the normal and tangential contact stiffness can be directly evaluated by the software or set up by the user. The main objective of the present research is to discuss the uncertainty associated with identifying with experimental data the normal and tangential stiffness in a dovetail coupling. In addition, the reliability of available theoretical contact models will be addressed. The response of the blade/attachment system was measured as a function of the axial load (simulating the centrifugal force) and of the blade vibration amplitude. An identification procedure using a finite element model was set up to identify the normal and tangential contact stiffness of the attachment. These stiffnesses were compared with the values predicted by a theoretical model. The comparison highlights a significant difference between measured and predicted stiffness. The final discussion focuses on the significance of theoretical contact stiffness and its use in finite element models.

1. Introduction

1.1. Background

Mechanical design of bladed disks in aero-engines includes the assessment of structural integrity against fatigue, be it high cycle, low cycle, or fretting fatigue [1–3]. To correctly predict stresses due to vibrations, accurate dynamic models are necessary. A complete resonance decoupling of such components is not a viable design choice because of the high modal density of the disk and the broad spectrum of the external loads. For this reason, damping introduced by dry friction is one of the tools used to reduce the amplitude of vibration. Friction damping develops at contact surfaces between shrouds, damper and under-platforms, disk slot and blade attachment, and more generally whenever interfaces are present.

Numerical simulations of models with interfaces are challenging because the tangential force in oscillating contacts is a piecewise function depending on the state of the contact, stick, slip or even separation of the surfaces. Researchers have been working

* Corresponding author.
E-mail addresses: daniele.botto@polito.it (D. Botto), matteo.glorioso@studenti.polito.it (M. Glorioso), serena.occhipinti@polito.it (S. Occhipinti), federica.cuccovillo@polito.it (F. Cuccovillo).

https://doi.org/10.1016/j.ymssp.2023.110379
Received 4 January 2023; Received in revised form 27 March 2023; Accepted 17 April 2023
Available online 2 May 2023

to develop efficient methods to solve the nonlinear equation of motion of dynamic systems embedding friction contacts. A new method, the harmonic balance technique, was proposed by in [4] to avoid the time domain solution of the dynamic equations of nonlinear circuits. This technique, known as Harmonic Balance Method (HBM), was widely used to determine the steady-state forced response of mechanical systems with nonlinear behavior [5]. An incremental HBM method, named as Multi-Harmonic Balance Method (MHBM), was developed in [6] for the analysis of damped systems with dry friction. In [7] this method was enhanced using a Fast Fourier Transform algorithm to transfer the equation of motion from time to frequency domain and vice versa. Nowadays, this technique is usually employed to study the dynamic behavior of bladed disks in turbomachines [8]. The method was improved with an analytical formulation of the contact forces [9] or by adding the static component of the contact force [10,11]. Time integration remains the most used tool to evaluate transients and even more efficient methods were put forward, see for example the one proposed in [12]. The aforementioned techniques make use of contact models based on Jenkins element in which the contact is composed by a linear spring in series with a Coulomb slider. Contact models evolved from the earlier one-dimensional [13] and two-dimensional [14] (2D) models to the more complete three dimensional frictional contacts [15] with variable normal load [16].

These models require three parameters to define the contact properties: the friction coefficient μ, the tangential and the normal contact stiffness, k_t and k_n respectively. The normal contact stiffness k_n for non-conforming geometries can be calculated with the Hertz theory as reported in [17]. The normal contact deformation of cylinders, despite their simple geometry, is a challenging task and several solutions are available in the literature [18–20]. The most reliable solution, supported by experimental tests, is the one proposed in [21]. The Hertz theory of contact was extended to account for friction forces and calculate the tangential stiffness between spherical bodies [22,23]. The solution for the contact of nonspherical bodies subjected to oblique loading was given in [24]. Among conforming geometries the rigid punch with rounded edges has a very important practical application in aero-engines because it is similar to the contact between the lobes in the disk slot and in the blade root. The pressure distribution was given in [25] for a friction-less rigid punch on an elastic half-space, while the effect of a tangential force on the state of stress was studied in [26]. The latter determined the boundary between stick and slip regions and the traction distribution. The theory presented in [26] was developed for 2D geometries and subsequently extended to three-dimensional (3D) contact bodies in [27]. This paper presents a semi-analytical method to evaluate the tangential force and displacements for a 3D punch with rounded edges. The contact stiffness and the dissipated energy are determined from the hysteresis loop (the friction force against the tangential displacement), provided the friction coefficient is known. The contact stiffness was also evaluated in its complex form by using an harmonic balance so that the imaginary part of the complex stiffness, that is in phase with the velocity [28], represents the damping effect. Calculation of damping induced by dry friction at blade attachments is still an open issue as evidenced by recent papers found in the literature [29,30].

Several experimental works, belonging to the field of micro-scale investigations, aimed at measuring the contact parameters for various geometries, materials and operating conditions. The first experimental investigations were performed in [17,31] using point contacts geometries to measure the relationship between the tangential force and the micro-displacement. [32] measured the hysteresis loop and the dissipated energy in the contact and underlined the importance of friction damping and its dependency on normal load. The experimental results were found to agree well with the previous analytical works [17,31]. The hysteresis loops for point contacts were also measured with a more recent test apparatus [33] and at the high temperatures typical of the aero-engine [34,35]. Conformal frictional contacts, characteristic of shrouds and disk-blade joints, were experimentally analyzed in [36,37] that investigated a pair of flat contact surfaces for several materials. A test rig working at high temperatures and capable to perform fretting test on flat-on-flat surfaces was proposed in [38]. An original approach to model friction contacts was given in [39] while several experimental tests were performed in [40–42].

Specific experimental campaigns were carried out to investigate the component-scale dynamic behavior of blades fixed with typical blade-disk joints. These campaigns provided a useful database for the validation of numerical simulations. The free response of a pulled mock-blade fixed with dovetail and fir-tree joints at its two ends was obtained in [43,44] . Damping and resonance frequencies were extracted as functions of the amplitude of vibration for different centrifugal loads. The same test rig was used in [45] to measure the forced-response and to collect a database of the frequency response with different normal contact loads and varying the dynamic excitation. A similar test apparatus [46] was used to measure the damping introduced by the blade-disk attachment. The joint behavior was simulated with two different contact models, one considering only macroslip conditions the other based on microslip. Results showed that the macroslip model was not suitable for accurate simulations. The damping ratio and the natural frequency on a simple beam with dovetail root joint was also measured in [47]. The centrifugal load was applied with a loading screw pushing on the back of the dovetail while a vibration slip table provided the dynamic excitation of the whole system. The micro-slip characteristic and the tangential contact stiffness were measured on the same material by using a fretting test rig. The contact stiffness inferred from the dynamic test performed on the simple beam with dovetail was compared with the results from the fretting test. Results showed that the tangential contact stiffness measured on the dovetail is smaller than the stiffness obtained by the fretting tests. The friction coefficient was measured on a fir-tree attachment in [48], but the rig used in this work did not allow measuring the contact stiffness.

1.2. Objective and workflow

Although the elastic properties of the contact in blade attachments are of great significance for engineers few works were devoted to measuring these parameters under dynamic conditions. The objective of the present work is to evaluate the uncertainty associated to the experimental identification of the contact stiffnesses k_n and k_t, along the normal and tangential direction, in a dovetail attachment. Moreover, the contact stiffnesses are also evaluated with the semi-analytical models found in the literature

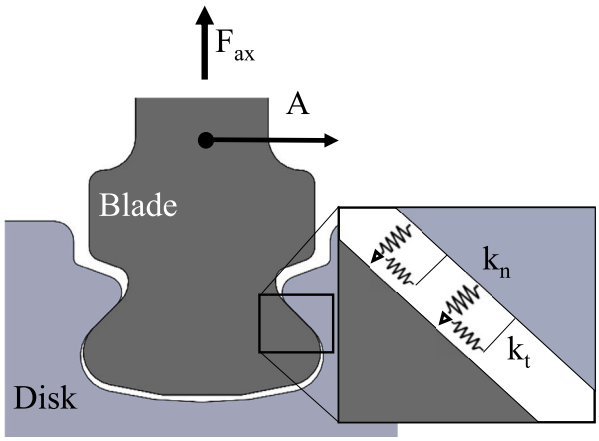

Fig. 1. Sketch of the dovetail joint investigated in this paper. The contact stiffnesses are highlighted in the panel.

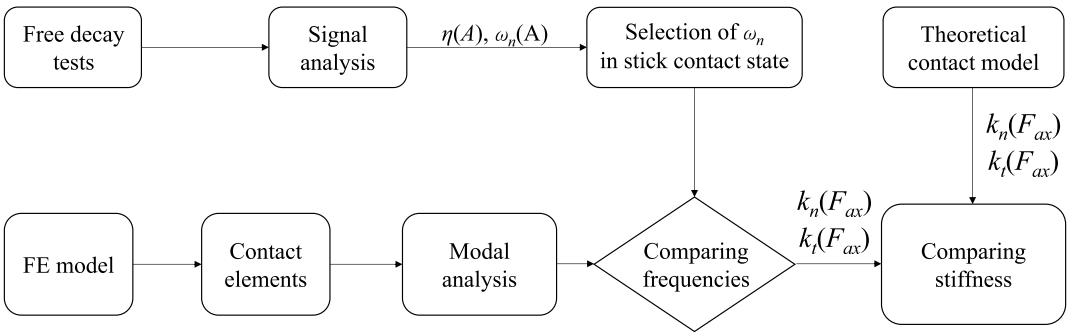

Fig. 2. Overview of the different phases of the activity.

and compared with the experimental results. This comparison was aimed to asses if the elastic contact parameters calculated with these models are feasible as contact elements in a FE model during the design step of bladed disks. The objective is pursued by collecting the dynamic response of a mock-blade with dovetail joints, as depicted in Fig. 1, and analyzing the results with the help of a FE model. The flow chart in Fig. 2 shows the analysis procedure described in detail below.

- Section 2 reports the main findings of the method proposed in [49] to identify the instantaneous natural frequency $\omega_n(A)$ and the instantaneous damping $\eta(A)$ depending on the vibration amplitude A. More details on the method are given in [50] while properties and assumptions regarding the Hilbert transform can be found in [51]. The reader familiar with the method can skip this section.
- Section 3 describes the experimental apparatus used for the dynamic tests on the mock-blade. This apparatus utilizes the rig described in [43] but in this work a different excitation system is used. The free decay of the mock-blade is measured for different tensile axial forces F_{ax} and then processed to extract ω_n and η of the nonlinear system.
- Section 4 illustrates the FE model of mock-blade and supports. Contact elements containing the unknown stiffnesses k_t and k_n connect the corresponding contact nodes on the dovetail and on the slot. These elements implement only the stick state. This section also reports the method used to obtain the reduced models of the mock-blade and supports, comprehensive of the stiffening effect due to the axial force.
- Section 5 describes how the theoretical contact stiffnesses in the attachment k_t^{th} and k_n^{th} can be calculated using the semi-analytical model of the flat punch with rounded edges proposed in [27]. The theoretical and experimental results are compared to discuss the feasibility of the theoretical model for the blade design.
- Section 6 documents the procedure to identify k_n and k_t for varying F_{ax}. The experimentally determined natural frequencies are compared with the frequencies computed by the FE model modal analysis. Appendix reports the uncertainty of the identified stiffness.

Throughout this paper boldface letters indicate vectors and matrices. Moreover, the greek letter ω indicates frequencies in rad/s whereas f is the frequency expressed in Hz.

2. Frequency and damping identification

The dependence of the natural frequency and damping on the amplitude of vibration, typical of nonlinear behavior, can be obtained from a free decay test with the method proposed in [49]. This method works in the time domain and is based on the analytic signal *Y(t)* corresponding to the real signal *y(t)*

$$Y(t) = y(t) + i\tilde{y}(t) = A(t) \cdot e^{i\varphi(t)} \tag{1}$$

where $\tilde{y}(t)$

$$\tilde{y}(t) = H[y(t)] = \frac{1}{\pi t} * y(t) = \frac{1}{\pi} \int_{-\infty}^{+\infty} \frac{y(t)}{t-\tau} d\tau \tag{2}$$

is the Hilbert transform of *y(t)*. The terms *A(t)* and $\Phi(t)$ in Eq. (1) are the instantaneous amplitude and instantaneous phase of the analytic signal *Y(t)* respectively.

Dry friction is the dominant source of damping in blade attachments. Friction forces undergoing oscillating motion generate hysteresis loops as sketched in Fig. 4(b). Analysis of energy dissipation in hysteresis loops lead to the conclusion that dry friction can be classified as a frequency-dependent damping. This kind of damping is denoted to as hysteretic damping and in dynamic model it is equivalent to an imaginary stiffness. The dynamic equation of motion with hysteretic damping can be written as

$$m\,\ddot{y} + (k(A) + i\,h(A))\,y = 0 \tag{3}$$

In Eq. (3) the stiffness *k(A)* and the hysteretic damping *h(A)* are unknown functions and, for nonlinear systems, depend on the amplitude of vibration *A*. Applying the Hilbert transform to Eq. (3) the dynamic equation of motion becomes

$$m\,\ddot{\tilde{y}} + (k(A) + i\,h(A))\,\tilde{y} = 0 \tag{4}$$

Multiplying each term of Eq. (4) by the imaginary unit *i* and adding it to the corresponding term of Eq. (3) we obtain the analytic form of the equation of motion

$$m\,\ddot{Y} + (k(A) + i\,h(A))\,Y = 0 \tag{5}$$

Eq. (5) can be rewritten

$$\ddot{Y} + \omega_n^2(A)\,(1 + i\,\eta(A))\,Y = 0 \tag{6}$$

with

$$\omega_n^2(A) = \frac{k(A)}{m} \tag{7a}$$

$$\eta(A) = \frac{h(A)}{k(A)} \tag{7b}$$

the instantaneous natural frequency and the loss factor respectively, also referred to as modal parameters. The first and second derivative of the analytic signal in Eq. (1) are

$$\dot{Y} = \dot{y} + i\dot{\tilde{y}} = (y + i\tilde{y})\left[\frac{\dot{A}}{A} + i\omega\right] \tag{8a}$$

$$\ddot{Y} = \ddot{y} + i\ddot{\tilde{y}} = (y + i\tilde{y})\left[\frac{\ddot{A}}{A} - \omega^2 + i2\omega\frac{\dot{A}}{A} + i\dot{\omega}\right] \tag{8b}$$

where $\omega = \dot{\varphi}(t)$ is the instantaneous frequency of the signal. By substituting Eq. (8b) into Eq. (5) the dynamic equation of motion becomes

$$\left[\frac{\ddot{A}}{A} - \omega^2 + \omega_n^2 + i\left(2\omega\frac{\dot{A}}{A} + \dot{\omega} + \omega_n^2\eta\right)\right] Y = 0 \tag{9}$$

By solving two equation for the real and imaginary parts of Eq. (9) we obtain the expression for the two unknown parameters

$$\omega_n^2(A) = \omega^2 - \frac{\ddot{A}}{A} \tag{10a}$$

$$\eta(A) = -\frac{1}{\omega_n^2}\left(2\omega\frac{\dot{A}}{A} + \dot{\omega}\right) \tag{10b}$$

The terms on the right-hand side of Eqs. (10) can be evaluated using the measured signal *y(t)* and its Hilbert transform $\tilde{y}(t)$. The first derivative (Eq. (8a)) gives the free vibration frequency ω and the ratio $\dot{A}/A$

$$\omega(t) = \frac{1}{A^2}\left(y\dot{\tilde{y}} - \dot{y}\tilde{y}\right) \tag{11a}$$

$$\frac{\dot{A}}{A}(t) = \frac{1}{A^2}\left(y\dot{y} + \tilde{y}\dot{\tilde{y}}\right) \tag{11b}$$

while the second derivative (Eq. (8b)) gives the variation of free vibration frequency $\dot{\omega}$ and the ratio $\ddot{A}/A$

$$\dot{\omega}(t) = \frac{y\dddot{y} - \tilde{y}\ddot{y}}{A^2} - 2\omega\frac{\dot{A}}{A} \tag{12a}$$

$$\frac{\ddot{A}}{A}(t) = \frac{y\ddot{y} + \tilde{y}\dddot{y}}{A^2} + \omega^2 \tag{12b}$$

The right-hand side in Eqs. (11) and (12) depends on the Amplitude $A(t)$ that can be evaluated as

$$A(t) = \sqrt{y^2 + \tilde{y}^2} \tag{13}$$

3. Experimental measurements

3.1. Test rig

Fig. 3 depicts the working scheme of the test rig used in the present work. The complexity of generating the centrifugal load through a rotating rig led to the development of a static loading technique. The unfeasibility of statically pulling a real blade without introducing additional damping is the reason of the symmetry of the rig, in which a dovetail type attachment is machined at both ends of a beam with constant rectangular cross-section to create the mock-blade. The equivalence of loads and joint kinematics makes the results obtained on this rig comparable with those on a real disk. More detailed considerations on the design principle of the rig can be found in [43].

The attachments are fitted into the slots machined in two supports. These supports are integral with two crossbars: one crossbar is fixed while the other is free to move if loaded with an axial force. The axial force F_{ax} is exerted through a hydraulic cylinder operated by a manual pump. The axial force is measured with two independent systems. A pressure gauge is connected to the hydraulic cylinder and its value is read directly by the operator. A full-bridge strain gauge is attached with adhesive to the mock-blade and it is read by a signal conditioning card and stored by the Data AcQuisition (DAQ) system. The dynamic excitation system is composed by an electrodynamic shaker and its power amplifier. This amplifier is fed with a signal produced by a wave form generator. The drive rod of the shaker is not fixed to the mock-blade but it can be brought into contact or released by displacing the moving coil of the shaker. Beforehand, the drive rod is displaced by a wave form consisting of a ramp followed by a positive constant value. A proper choice of the initial gap between the drive rod and the mock-blade together with the value of the constant signal allows the drive rod to preload the mock-blade. The preload is followed by a sinusoidal wave whose frequency is chosen as close as possible to the resonance of the modal shape under investigation. If the preload has been properly defined the drive rod remains in contact with the mock-blade during the sinusoidal excitation period. At the end of the excitation period the drive rod is suddenly detached, with a negative wave form signal, from the mock-blade that from this point on is free to oscillate so that no additional damping injected by the shaker. This method will be referred to as the Detached Drive Rod Method (DDRM). The excitation system used in this work differs from the one used in [43] in which the mock-blade was loaded with a non-contact exciter based on electromagnets. The main objective of both systems is the same: to uncouple the mock-blade from the exciter so that no additional damping is injected during the free decay. With the non-contact exciter this objective is achieved by stopping the current in the coil whereas with the DDRM the drive rod is physically detached from the contact point. The main advantage of using the DDRM is that the excitation force is applied at a specific point and can be measured with a load cell if the forced-response is needed. The non-contact exciter needs a complex calibration process to measure the transfer function between the force measured on the electromagnet and the true force applied to the mock-blade, as well explained in [45].

A Laser Doppler Vibrometer together with its controller measures the velocity of one reference point at time on the mock-blade. The DAQ system collects and records point velocity and strain gauge signals. The wave form is created with a in-house code with a sampling rate of 10 kHz and stored on file. This file is then read by the wave form generator that provides the output voltage signal.

3.2. Testing procedure

Experiments were focused on the free decay of oscillations of the first and second bending mode of the mock-blade. Velocity was measured at the antinode of the modal shape under investigation. For both modes a set of measurements at different axial loads F_{ax} was carried out. The testing procedure for each measurement is described in the following.

1. The mock-blade is pulled with the axial load F_{ax}, which is evaluated with the pressure gauge and strain gauges through the formulae

$$F_{ax} = A_{cyl}\, p \tag{14a}$$

$$F_{ax} = A_{beam}\, \sigma = A_{beam}\, E_{st}\, \epsilon \tag{14b}$$

where $A_{cyl} = 1790$ mm^2 is the effective area of the hydraulic cylinder, p is the measured pressure, $A_{beam} = 26 \times 10$ mm^2 is the rectangular cross-section of the mock-blade, $E_{st} = 200.3$ GPa the Young Modulus of the blade material (steal) and ϵ the measured strain. The total length of the blade is 325.7 mm, comprehensive of the dovetail extremities, see Fig. 9(a). As reported in [43], on real engines in cruise condition a typical centrifugal load on blades is about 50 kN. The minimum load, during the flight descent phase when the engine runs at idle speed, is about 2.5 kN. In the present work measurements were performed with tensile loads up to 25 kN, a value that is representative of the real operating condition.

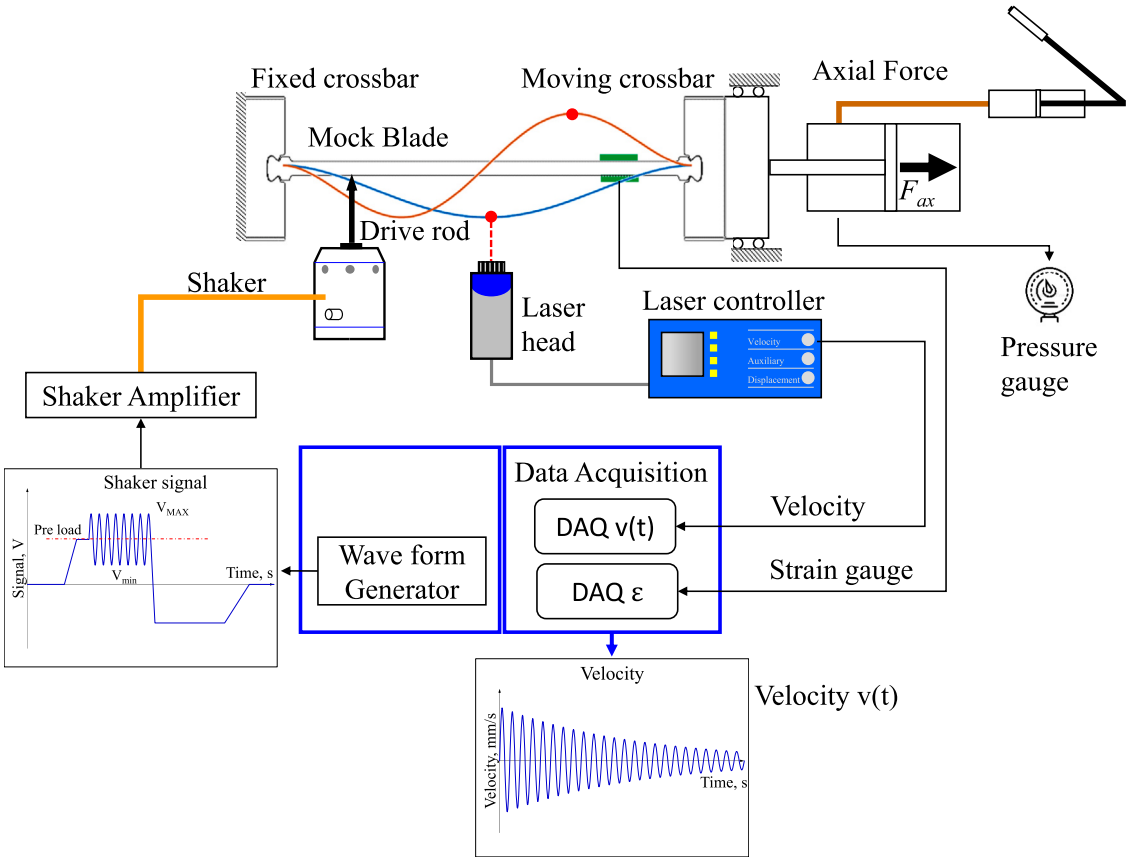

Fig. 3. Test Rig scheme.

2. A preliminary hammer test is performed on the loaded mock-blade to obtain a first estimate of the natural frequencies of the first two bending modes.
3. The loaded mock-blade is excited by using the DDRM with an oscillating force whose frequency was estimated as in point List 2. The free vibrations is obtained once the drive rod is detached from the excitation point.
4. The useful portion of the velocity *v(t)* is limited to the time interval of free decay. This portion of the signal is filtered with a bandpass Parks–McClellan FIR filter, centered on the frequency of the examined mode, to reduce noise and other undesired signals.
5. The measured signal is then processed with the method described in Section 2. In the present work, the measured signal is the velocity $v(t) = \dot{y}(t)$. Thus, displacement $y(t)$ and acceleration $\ddot{y}(t)$ were computed by numerical integration and differentiation of *v(t)* respectively.

3.3. Test results

Figs. 5 and 6 show the instantaneous frequency and loss factor of the first and second bending mode respectively. These dynamic parameters are evaluated with Eq. (10). Results are shown as functions of the displacement amplitude A of the antinode. In both modes frequency and loss factor are constant for small vibration amplitudes, see the detail in Fig. 5(b), thus revealing a linear behavior of the system. For small amplitudes slip is negligible whereas slip occurs for higher amplitudes. The loss factor shows a maximum, clearly visible in Fig. 5(b), at an optimal amplitude A_{opt}: before A_{opt} the loss factor increases whereas after A_{opt} it decreases. This maximum is not visible for the second mode, Fig. 6(b), because the output force available at the shaker was not able to displace the second mode up to the optimal amplitude. Oscillating displacements under slip condition lead to the formation of hysteresis loops as shown in Fig. 4(b). Friction at interfaces dissipates energy, the amount of which is related to the loop area that varies with the amplitude A. The maximum loss factor is found at the optimal amplitude that is not the maximum amplitude.

The loss factor, see Figs. 5(b) and 6(b), decreases with increasing axial loads F_{ax}, provided the amplitude is the same. This behavior is due to the increasing contact normal load N which reduces the gross-slip displacement range in the hysteresis loop, thus decreasing the dissipated energy. The natural frequency increases with axial loads F_{ax}, as reported in Figs. 5(a) and 6(a). This

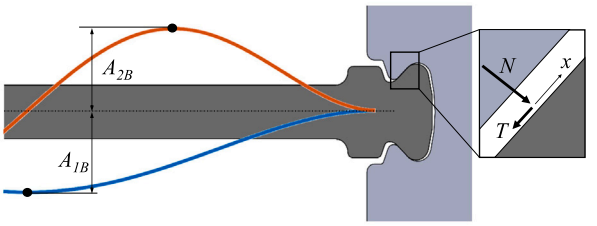

(a) First (1B) and second (2B) Bending modes of the mock-blade. A_{1B} and A_{2B} are the displacement amplitude of their respective antinodes. In the detail the tangential T and normal N contact force and the relative displacement x at interfaces.

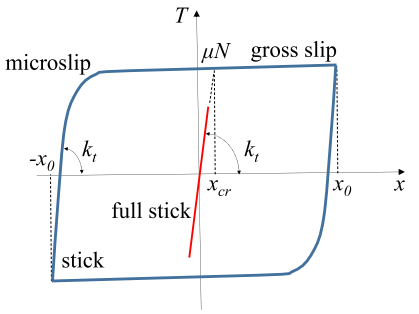

(b) Scheme of the Hysteresis loop between tangential force T and relative displacement x at contact interfaces. N: normal load; x_0: maximum amplitude of vibrating displacement x; k_t: contact tangential stiffness.

Fig. 4. Scheme of the first and second bending modes of the mock-blade, of the contact forces and hysteresis loop.

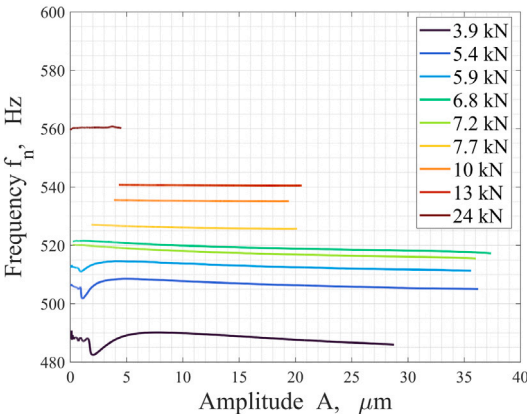

(a) Natural frequency.

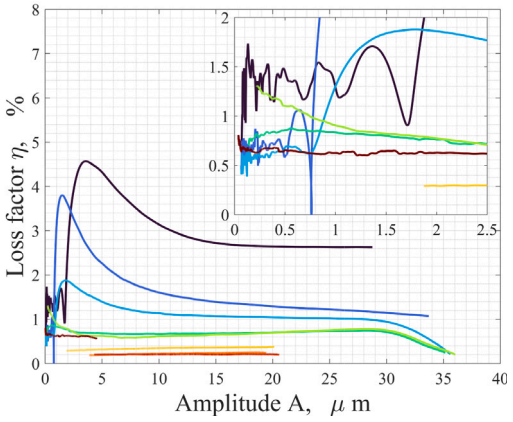

(b) Loss factor

Fig. 5. Modal parameters for the first bending mode (1B).

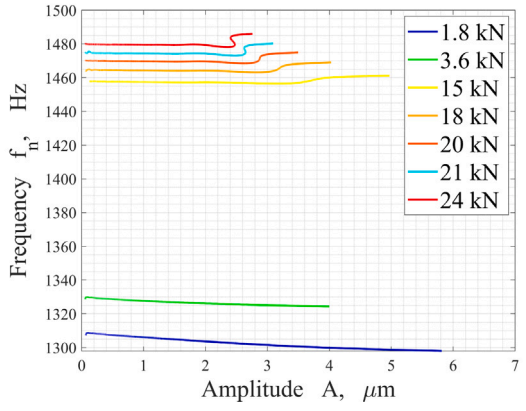

(a) Natural frequency.

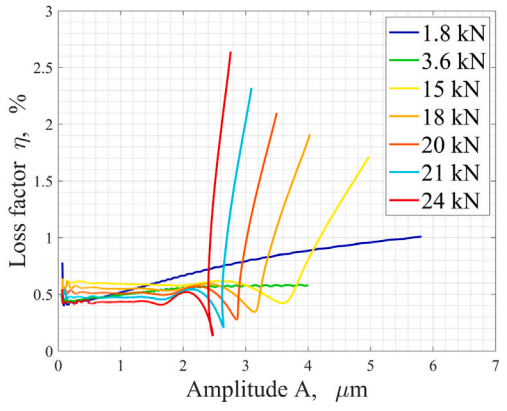

(b) Loss factor

Fig. 6. Modal parameters for the second bending mode (2B).

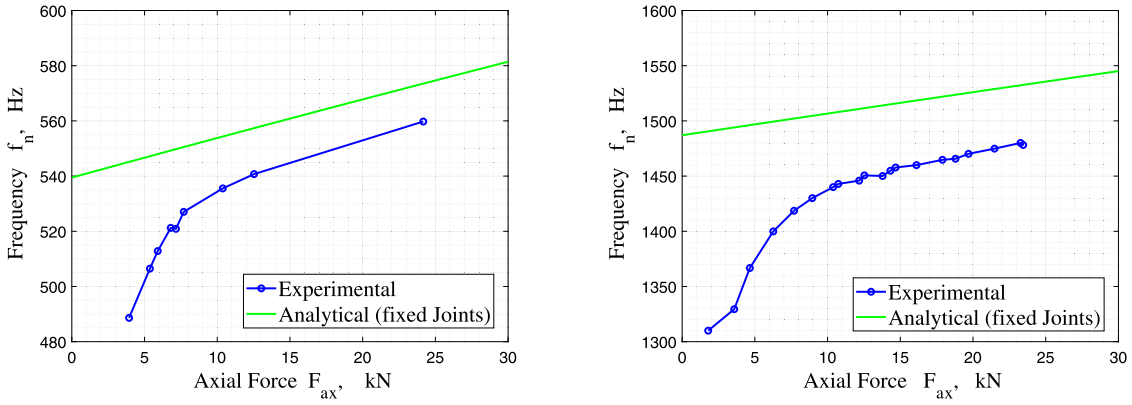

(a) Natural frequency of the first bending mode.

(b) Natural frequency of the second bending mode.

Fig. 7. Stiffening effect due to the axial load F_{ax}. The increase of the frequency predicted by the analytical model is compared with the experimental results.

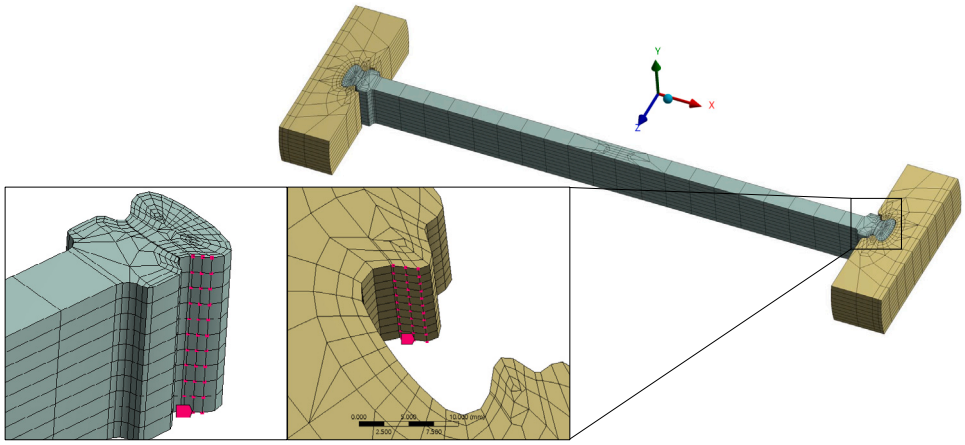

Fig. 8. Finite Element model and detail of contact nodes.

increment is caused by two factors. First, the axial stress along the beam produces a moment opposing the bending deformation. This effect was considered with an analytical model [52] in which the Euler–Bernoulli beam model was modified to introduce a second order deformation effects. The effect of F_{ax} on the frequencies, evaluated with this analytical model, is depicted in Fig. 7. The second effect is related to the increasing contact normal load N that increases the stiffness of the contacts. This phenomenon will be further discussed in Section 6. Fig. 7 also shows the natural frequencies measured in stick condition, taken as the mean value in the small amplitudes range. The measured frequency is lower than the predicted because the contact stiffness at the interfaces is in series with the mock-blade stiffness and then reduces the global stiffness. For axial loads greater than 12 kN the frequencies increase with a slope slightly higher than that predicted by the analytical model. For axial loads lower than 12 kN the experimental frequencies diverge from the theoretical ones because the interface tends to slip and the contact stiffness decreases, thus reducing the natural frequency of the entire system.

4. Finite element model

A commercial Finite Element (FE) model was used in the procedure to identify the normal and tangential contact stiffnesses. The mock-blade and the slots, depicted in Fig. 8, were modeled as separate bodies. The material properties of the mock-blade were evaluated with a hammer modal test in free-free condition. The measured modulus of elasticity and density were $E = 200.3$ GPa and $\rho = 7592$ kg/m^3 respectively. The contact surface on the root blade and the matching surface on the slot were discretized with the same number of nodes. These nodes have coincident coordinates, see the detail in Fig. 8, so that node-to-node contact element is allowed. These contact elements are assembled during the identification procedure.

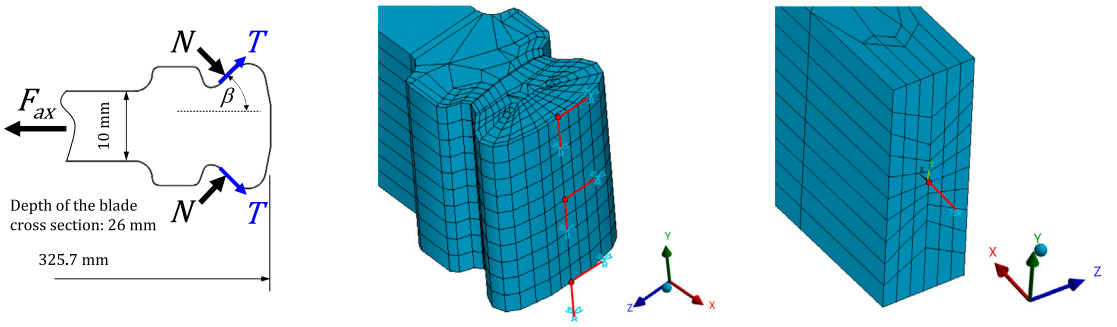

(a) Reaction forces on the dovetail contact interfaces along the normal N and tangential T directions.

(b) Soft spring at the mock-blade ends.

(c) Soft spring in the center cross-section of the mock-blade.

Fig. 9. Boundary conditions for the preliminary FE static analysis of the mock-blade.

4.1. Tensile force stiffening effect

The stiffening effect induced by the axial load F_{ax} was considered introducing the so-called geometrical stiffness matrix $\Delta\,\mathbf{K}_G$

$$\mathbf{K} = \mathbf{K}_0 + \Delta\mathbf{K}_{G,F_{ax}} \tag{15}$$

This matrix depends on the state of stress in the beam, and it was evaluated through a FE preliminary static analysis of the mock-blade for each F_{ax} applied in the experiments

$$\Delta\mathbf{K}_{G,F_{ax}} = \int_V \mathbf{S}_g^T \boldsymbol{\sigma} \mathbf{S}_g \, dV \tag{16}$$

In Eq. (16) $\boldsymbol{S}_g$ is the matrix of the shape functions derivatives while σ is the stress state matrix. The stress stiffening effect is only significant in slender bodies, then it was calculated for the mock-blade but not for the supports.

The preliminary static analysis was performed by applying to the dovetails contact surfaces the normal forces N balancing the axial load F_{ax}

$$N = \frac{F_{ax}}{2\sin\beta} \tag{17}$$

with $\beta = 45°$as sketched in Fig. 9(a). Since results are little affected by contact tangential forces T these forces were neglected. The mock-blade must be properly constrained during the preliminary analysis to avoid kinematic indeterminacy that would not allow solving the static problem. Since these constraints are embedded in the stiffness matrix in Eq. (15) they could invalidate the identification procedure of k_n and k_t. To avoid this issue the FE model was constrained with node-to-ground elastic springs with a very small stiffness $k = 1{\cdot}10^{-4}$ N/mm so that they have no effect on the mock-blade dynamics in the frequency range of interest. Three nodes for each dovetail were constrained along the transverse directions, see Fig. 9(b), while the center node of the mock-blade was constrained along the axial direction as in Fig. 9(c). The rigid motion of the mock-blade is canceled with a minimum number of constraints and complying with the symmetry of the first two modal shapes.

4.2. CMS reduction

The identification of the contact stiffness was performed with a purposely developed in-house code. This code utilizes the stiffness and mass matrix generated by the FE commercial software. To decrease the computational cost and speed up the identification process the Degrees of Freedom (DoF) of the models were reduced using the tool built in the FE software. Then the reduced matrices were exported in a suitable format and read by the in-house code. The reduction was performed with the Component Mode Synthesis (CMS), a technique developed in [53] for sub-structuring, and summarized in the following. The dynamic equations in physical coordinates $\mathbf{u}$ is

$$\mathbf{M}\ddot{\mathbf{u}} + \mathbf{K}\mathbf{u} = \mathbf{0} \tag{18}$$

The physical DoFs are divided in active $\mathbf{u}_a$ and omitted $\mathbf{u}_o$

$$\mathbf{u} = \begin{Bmatrix} \mathbf{u}_a \\ \mathbf{u}_o \end{Bmatrix} \tag{19}$$

so that Eq. (18) can be rearranged as

$$\begin{bmatrix} \mathbf{M}_{aa} & \mathbf{M}_{ao} \\ \mathbf{M}_{oa} & \mathbf{M}_{oo} \end{bmatrix} \begin{Bmatrix} \ddot{\mathbf{u}}_a \\ \ddot{\mathbf{u}}_o \end{Bmatrix} + \begin{bmatrix} \mathbf{K}_{aa} & \mathbf{K}_{ao} \\ \mathbf{K}_{oa} & \mathbf{K}_{oo} \end{bmatrix} \begin{Bmatrix} \mathbf{u}_a \\ \mathbf{u}_o \end{Bmatrix} = \mathbf{0} \tag{20}$$

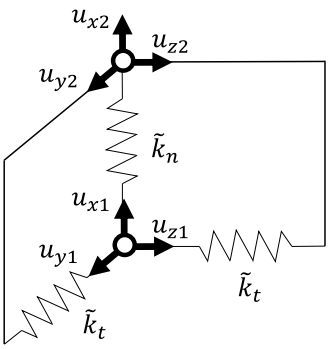

$$\boldsymbol{K}_e^L = \begin{bmatrix} \tilde{k}_n & 0 & 0 & -\tilde{k}_n & 0 & 0 \\ & \tilde{k}_t & 0 & 0 & -\tilde{k}_t & 0 \\ & & \tilde{k}_t & 0 & 0 & -\tilde{k}_t \\ & & & \tilde{k}_n & 0 & 0 \\ & symm & & & \tilde{k}_t & 0 \\ & & & & & \tilde{k}_t \end{bmatrix} \qquad \boldsymbol{u}^L = \begin{Bmatrix} u_{x1} \\ u_{y1} \\ u_{z1} \\ u_{x2} \\ u_{y2} \\ u_{z2} \end{Bmatrix}$$

Fig. 10. Node-to-node contact element. $\tilde{k}_n$ and $\tilde{k}_t$ are the nodal stiffnesses.

According to the CMS method, only the physical displacement $\boldsymbol{u_a}$ of the active nodes are retained in the equation. The omitted DoFs are approximated with a linear combination of the active DoFs and normal modes $\boldsymbol{\Phi}_{oo}$

$$\mathbf{u} = \begin{Bmatrix} \mathbf{u}_m \\ \mathbf{u}_s \end{Bmatrix} = \begin{bmatrix} \mathbf{I} & \mathbf{0} \\ \mathbf{K}_{oo}^{-1}\mathbf{K}_{oa} & \overline{\boldsymbol{\Phi}}_{oo} \end{bmatrix} \begin{Bmatrix} \mathbf{u}_a \\ \boldsymbol{\eta}_o \end{Bmatrix} = \mathbf{T}\mathbf{q} \tag{21}$$

The normal modes $\boldsymbol{\Phi}_{oo}$ are solution to the eigenproblem of the sub-system composed of the omitted DoFs with proper boundary conditions. $\overline{\boldsymbol{\Phi}}_{oo}$ is a subset of $\boldsymbol{\Phi}_{oo}$ while $\boldsymbol{\eta}_o$ are the modal DoFs. The number of active and modal DoFs defines the degree of reduction. The dynamic Eq. (18) becomes

$$\overline{\mathbf{M}}\ddot{\mathbf{q}} + \overline{\mathbf{K}}\mathbf{q} = \mathbf{0} \tag{22}$$

with $\mathbf{q}$ generalized DoFs and

$$\overline{\mathbf{K}} = \mathbf{T}^T\mathbf{K}\mathbf{T} \tag{23a}$$

$$\overline{\mathbf{M}} = \mathbf{T}^T\mathbf{M}\mathbf{T} \tag{23b}$$

are the reduced stiffness and mass matrices. The reduction was performed separately for the mock-blade and the two supports. The mock-blade stiffness matrix is actually a set of matrices, one for each axial load F_{ax}, according to what reported in Section 4.1. The active nodes on the mock-blade comprise 33 nodes on each contact interface and two line of 21 nodes each along the axial direction. These nodes allow visualizing the modal shapes during post processing of the results. One of these latter nodes coincides with the spot on which the velocity is measured, another one with the excitation point. The subset $\overline{\boldsymbol{\Phi}}_{oo}$ is composed by the first 100 modal shapes (corresponding to the lowest frequencies) which brings the total number of generalized DoFs to 622. The active nodes on the support are the nodes on the contact interfaces and 117 nodes on the base. The latter nodes allow a static analysis of the reduced model of the support. This analysis was not performed in the present work and these DoFs were constrained. Also for the support 100 modal shapes were chosen so that the number of generalized DoFs amounts to 322.

4.3. Contact element

The mock-blade roots and the supports are connected by node-to-node contact elements, namely springs acting along the normal and tangential directions of the contact surface. The stiffness of these nodal springs $\tilde{k}_n$ and $\tilde{k}_t$ are obtained by uniformly distributing the contact stiffness of the attachment k_n and k_t on the nodes of each interface. The contact element and its stiffness matrix and DoFs in the Local coordinate system are visible in Fig. 10.

5. Semi-analytical contact model

The unknown contact stiffnesses k_n and k_t were identified following the procedure described in Section 6. Nevertheless, the contact stiffness can be also estimated by using the semi-analytical solution of the contact between a flat punch on an infinite half-plane, as shown in Fig. 11(a). These stiffnesses are referred to as theoretical contact stiffnesses k_n^{th} and k_t^{th}. The pressure distribution p on a punch with rounded edges

$$\frac{bp(\phi)}{P} = \frac{2/\pi}{\pi - 2\phi_0 - \sin 2\phi_0}\left[(\pi - 2\phi_0)\cos\phi + \sin\phi \ln\left|\frac{\sin(\phi+\phi_0)}{\sin(\phi-\phi_0)}\right| + \sin\phi_0 \ln\left|\tan\frac{\phi+\phi_0}{2}\tan\frac{\phi-\phi_0}{2}\right|\right] \tag{24}$$

was first found in [25] and also recalculated in [26]. Eq. (24) is given in dimensionless form in which b is the contact half-width and P the normal load per unit length. Fig. 11(a) sketches the analogy between the punch geometry and the contact region in the

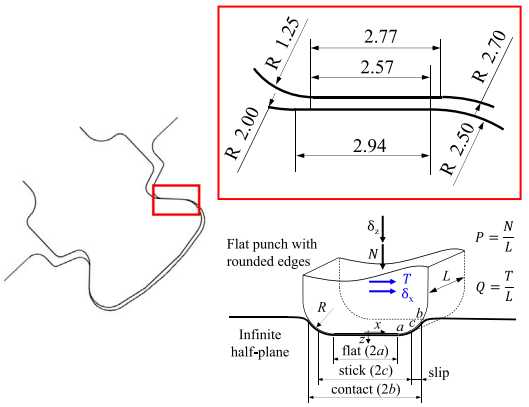

(a) Scheme of the punch with rounded edges.

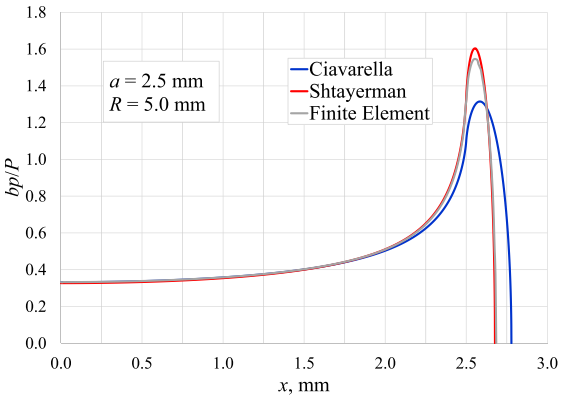

(b) Pressure distribution computed with different analytical model compared with the FE solution.

Fig. 11. The punch with rounded edges and its pressure distribution.

attachment. The auxiliary angle ϕ is defined as $\sin\phi = x/b$ and the angle ϕ_0 implicitly specifies the half-width $b = a/\sin\phi_0$. The angle ϕ_0 can be found by solving the equation

$$\frac{nPR}{a^2E^*} = \frac{\pi - 2\phi_0}{2\sin^2\phi_0} - \cot\phi_0 \tag{25}$$

where $2a = 2.57$ mm and $1/E^* = \sum_{i=1,2}(1-\nu_i^2)/E_i$ with $E_i = 200.3$ GPa and $\nu_i = 0.3$ the Young's modulus and the Poisson's ratio of the i-body. The contact length is $L = 26$ mm while the curvature radius of the rounded edges is $R = 2.50$ mm (considering a symmetrical punch geometry). Because the real profile is not symmetric R was chosen as the maximum between the two radius (1.25 and 2.50 mm) corresponding to the higher values of the contact stiffnesses k_n^{th} and k_t^{th}. However, the variation of the theoretical contact stiffness with the radius R in the above-mentioned range is negligible.

A discrepancy was found about the coefficient n in Eq. (25): according to [25] $n = 2$ whereas [26] reports a coefficient $n = 4$. Fig. 11(b) shows the pressure distribution calculated with the two different coefficients and compares it with the results of a FE analysis. The coefficient $n = 4$ overestimate the contact half-width and coherently underestimate the pressure peak. For this reason, this work utilizes the formulation proposed in [25].

The results obtained in [25] were extended in [26] in the case of contacts experiencing also a tangential force T. The shear stress was calculated as the sum of the stress in full slip condition $\mu p(x)$ (μ being the friction coefficient) and a corrective shear stress $q^*(x)$ in the stick region

$$q(x) = \mu p(x) - q^*(x) \tag{26}$$

The corrective shear stress distribution $q^*(\theta)$ is

$$\frac{cq^*(\theta)}{\mu P - Q} = -\frac{2/\pi}{\pi - 2\theta_0 - \sin 2\theta_0}\left[(\pi - 2\theta_0)\cos\theta + \sin\theta\ln\left|\frac{\sin(\theta+\theta_0)}{\sin(\theta-\theta_0)}\right| + \sin\theta_0\ln\left|\tan\frac{\theta+\theta_0}{2}\tan\frac{\theta-\theta_0}{2}\right|\right] \tag{27}$$

where $\sin\theta = x/c$, $P = N/L$ and $Q = T/L$. The half-width of the stick region $c = a/\sin\theta_0$, see Fig. 11(a), is computed solving for θ_0 in the equation

$$\frac{nPR}{a^2E^*}\left(1 - \frac{Q}{\mu P}\right) = \frac{\pi - 2\theta_0}{2\sin^2\theta_0} - \cot\theta_0 \tag{28}$$

The tangential displacement δ_x was found in [27]

$$\delta_x = u_{x1} - u_{x2} = \frac{2}{\pi E^*}\left[-\int_{-b}^{b} q_x(r)\ln\left|\frac{r}{b}\right| dr + Q\left(\ln\left|\frac{L}{b}\right| + \frac{\nu}{1-\nu}\right)\right] \tag{29}$$

through the elastic potential theory of Boussinesq–Cerruti as reported in [54]. Hence, the stiffness is calculated as the first derivative of the tangential force at the onset of the tangential displacement for a given normal force N

$$k_t^{th}(N) = \left(\frac{\partial T}{\partial\delta_x}\right)_{\delta_x=0} = \frac{1}{\left(\frac{\partial\delta_x(N)}{\partial T}\right)_{T=0}} \tag{30}$$

Similarly, the normal displacement of each body is

$$|u_{z_i}| = \frac{1-\nu_i^2}{\pi E_i}\int_{-b}^{b} p(r)\left(\int_{-L/2}^{L/2}\frac{1}{\sqrt{r^2+s^2}}ds\right)dr = \frac{1-\nu_i^2}{\pi E_i}\int_{-b}^{b} p(r)2\sinh^{-1}\left(\frac{L/2}{|r|}\right)dr \tag{31}$$

thus the relative normal displacement δ_z is

$$\delta_z = u_{z1} - u_{z2} = \frac{2}{\pi E^*} \int_{-b}^{b} p(r) \sinh^{-1}\left(\frac{L/2}{|r|}\right) dr \tag{32}$$

and the normal contact stiffness can be written as

$$k_n^{th}(N) = \frac{\partial N}{\partial \delta_z} = \frac{1}{\frac{\partial \delta_z}{\partial N}} \tag{33}$$

For a given axial force F_{ax} the corresponding normal load N ranges from a minimum $N_{\min}$ (corresponding to full slip $T = \mu N$) and a maximum value $N_{\max}$ (corresponding to a friction-less contact $T = 0$)

$$\frac{F_{ax}}{2(\sin\beta + \mu\cos\beta)} \le N \le \frac{F_{ax}}{2\sin\beta} \tag{34}$$

as visualized in Figs. 9(a), 13(b) shows that the theoretical contact stiffness are weakly affected by the tangential force T with $\mu = 0.4$.

6. Contact stiffness identification

The unknown contact stiffnesses k_n and k_t were indirectly estimated through their influence on the natural frequencies calculated by the reduced FE model. These frequencies, calculated for both the first (1B) and second (2B) bending mode, were compared with the measured frequencies. This comparison was carried out for each axial load F_{ax} with which experiments were performed. The analysis was achieved for small vibration amplitudes in which gross slip does not occur. In this condition the frequency remains constant, as shown in Fig. 6(a), and the system exhibits a linear behavior. Microslip is always present but its influence is significant only for axial loads less than 12 kN, as reported in Fig. 7. For this reason, only results obtained with axial loads greater than 12 kN were employed in the comparison. The unknown stiffnesses k_n and k_t can be determined by solving at each axial load F_{ax} the nonlinear system

$$\left\{ \begin{array}{c} f^{FE}_{n,1B}(k_n, k_t) - f^{m}_{n,1B} \\ f^{FE}_{n,2B}(k_n, k_t) - f^{m}_{n,2B} \end{array} \right\} = \left\{ \begin{array}{c} \Delta f_{n,1B} \\ \Delta f_{n,2B} \end{array} \right\} = \left\{ \begin{array}{c} 0 \\ 0 \end{array} \right\} \tag{35}$$

where $\boldsymbol{f}_n^{FE}$ and $\boldsymbol{f}_n^{m}$ are the computed and measured natural frequencies respectively. The natural frequencies of the first bending mode as a function of the contact stiffness are shown in Fig. 12(a). Eq. (35) is solved by finding the locus of the minima of the residual norm $g := \|\Delta \boldsymbol{f}_n\|$. This locus is characterized by a minimum gradient $\|\nabla g\|$ on the level curves of the residual norm surface

$$\begin{cases} \frac{\partial}{\partial n}\|\nabla g\| = 0 \\ \frac{\partial^2}{\partial n^2}\|\nabla g\| > 0 \end{cases} \tag{36}$$

where direction $\boldsymbol{n}$ defines the level curve as $\nabla g \cdot \boldsymbol{n} = 0$. Together with Eq. (36) a further limit is set on the value of the norm that must be less than a selected tolerance $g < toll_g$. The locus of the minima can be visualized as the path followed by a sphere free to roll on the residual norm surface. This path is visualized by the solid line marked in Fig. 12(b). This locus represents the feasible solutions and is reported in Fig. 12(c) for different axial loads. Once the loci are defined a single solution must be selected. In this work the following three criteria were considered.

- The most intuitive criterion is to find the global minimum of $\|\Delta \boldsymbol{f}_n\|$ on the minima locus. The drawback of this criterion is the low accuracy with which the stiffness is determined. The errors on the stiffness, computed with the procedure described in Appendix, is about 55% and makes this solution less reliable. The reason for this large error is that the solution $(k_n, k_t) \simeq (1, 7)$ kN/μm belongs to the region in which the sensitivity of the contact stiffness to the frequency variation is high, and a small uncertainty on the measured frequencies propagates dramatically on the stiffness value.
- Uncertainty on the identified stiffness also suggests a different criterion: selecting the solution (k_n, k_t) with the minimum error (according to the procedure described in Appendix). This solution is denoted to as the "optimal solution pair".
- The theoretical contact stiffnesses were calculated in Section 5 and their values can guide the selection procedure. A third option is to choose the pair (k_n, k_t) with the minimum distance from theoretical stiffness.

Fig. 12(c) reports the solution determined with the last two criteria: these solutions are close to each other and almost equivalent. In this work, the optimal solution criterion was adopted and Table 1 reports the numerical results with their accuracy. The ratio of tangential to normal stiffness remains almost constant, $k_t/k_n \simeq 1.37$. This result differs from what reported in [55] in which this ratio slowly increases with normal loading.

Fig. 13(a) compares the optimal and the theoretical solution and points out that the difference between the two results is very high. Taking the theoretical stiffness as reference, the difference in the worst case is about 82% and 164% for k_n and k_t respectively. Furthermore, the trend of the two solutions at varying axial loads is very different. The optimal solution shows a slope of about 73 and 95 $\mathrm{Nmm^{-1}/N}$ for k_n and k_t respectively, whereas the theoretical values remains almost constant at varying axial load as emphasized in Fig. 13(b).

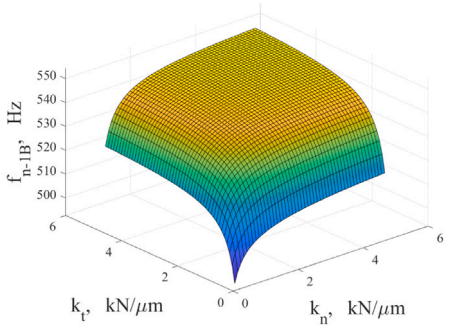

(a) Natural frequency as a function of contact stiffness; F_{ax}=12kN.

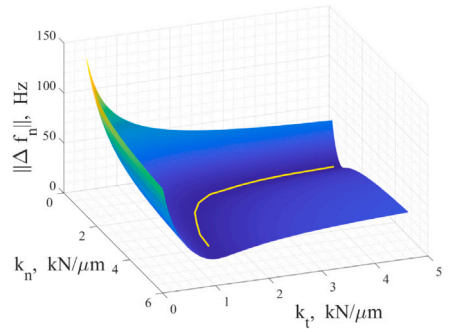

(b) Norm of residual as a function of contact stiffness; F_{ax}=12kN.

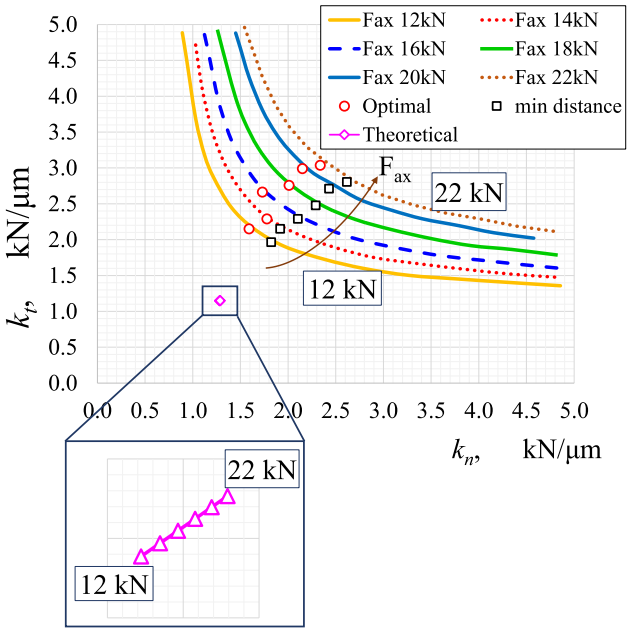

(c) Loci of feasible solutions at different axial loads F_{ax}. Solutions with minimum uncertainty and with minimum distance from the theoretical values.

Fig. 12. Variation of frequency (a) and residual norm (b) with contact stiffness. Loci of the minima with optimal and minimum distance solutions for different axial loads.

Table 1
Normal and tangential contact stiffness with their estimated errors for different axial loads.

F_{ax} kN	k_n kN/μm	σ_{nn}/k_n %	k_t kN/μm	σ_{tt}/k_t %
12	1.59	15	2.15	12
14	1.68	17	2.38	15
16	1.82	21	2.57	18
18	2.01	26	2.76	22
20	2.15	27	2.99	25
22	2.34	31	3.04	26

Most of this discrepancy is due to the slightly different meaning that the term “contact stiffness” takes on in the numerical and analytical models. In the numerical model, the optimal contact stiffness represents the local connection between the two bodies through the interface that breaks off the continuum. The flexibility of the bulk, here the lobes on root and slots, is considered in the finite element model. The global stiffness is given by the series of the optimal and bulk stiffness. On the contrary, the analytical model calculates the displacements, from which the theoretical stiffness are deduced, considering the elastic half-space. The comparison should be made between global and theoretical stiffness rather than optimal and theoretical stiffness, but this comparison is by no means an easy task.

Furthermore, the assumption of elastic half-space is valid only if the size *2b* of the contact region is much smaller than the curvature radius *R* [27], hypothesis not strictly fulfilled in the real contact geometry of the examined joint.

Moreover, the blade deformation and the lobe flexibility induce rotation of the contact surfaces. This rotation generates an asymmetric pressure distribution, whereas the theoretical model assumes that the loads and the pressure distribution are symmetric. Since the contact problem is nonlinear asymmetric pressure distributions result in different stiffness even for the same normal load. An analytical model comprehensive of the moment and asymmetry of the contact patch was put forward in [56]. This model delivers the pressure and tangential distribution, but the displacement field from which the contact stiffness is derived is not ready yet. Furthermore, it is not easy to evaluate the moment at the root when the blade is oscillating also considering that this moment varies during a cycle.

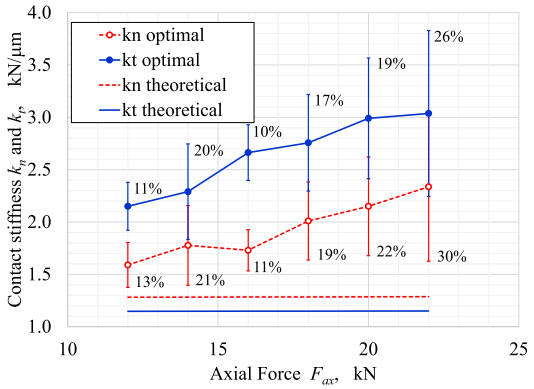

(a) Optimal and theoretical contact stiffness at different axial loads F_{ax}

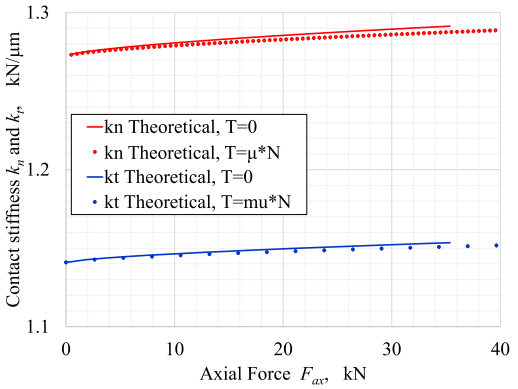

(b) Theoretical contact stiffness for friction-less contact (T=0) and with a friction coefficient $\mu = 0.4$.

Fig. 13. Comparison between the optimal contact stiffness resulting from the identification procedure and the theoretical values obtained with the semi-analytical model.

7. Conclusions

This paper has presented a novel procedure to experimentally investigate modal parameters, namely natural frequency and loss factor, in blade attachments. Experimental data were collected on a mock-blade with a dovetail at both ends. In our experiment, a shaker excited the mock-blade whose free decay was measured with a laser Doppler velocimeter. The Detached Drive Rod Method was developed to ensure that the free decay was not affected by any coupling with the excitation system. Results substantiate the dependency of the modal parameters on the vibration amplitude, a behavior typical of nonlinear systems. Results also show that the loss factor reaches a maximum, at an optimal amplitude, as predicted by theoretical models.

An in-house code was also developed to identify contact stiffness. The identification procedure was performed by comparing first- and second-mode natural frequencies calculated from an FE model with experimentally measured frequencies. The presence of two variables, namely normal and tangential stiffness, generates a multi-objective optimization problem. The main findings of the analysis are reported below.

- The objective function does not have a unique minimum but a locus of minima that does not allow a pair stiffness k_t and k_n to be uniquely identified. This result is reasonable, because these stiffnesses affect the first and second bending mode similarly and their effect on these modes cannot be clearly separated. With an arbitrary choice, the contact stiffness pair with minimum uncertainty was chosen among the feasible solutions and named "optimal stiffness pair".
- Better identification could be made by taking advantage of a theoretical contact model to guide the analysis. To this end the optimal stiffness pair was also compared with the theoretical stiffness calculated with a semi-analytical solution. The difference between the optimal and theoretical results is very high, reaching 82% and 164% in the worst case for k_t and k_n respectively. The trend of the contact stiffness at varying axial loads is also very different. The optimal stiffness showed a slope of about 73 and 95 $\mathrm{Nmm}^{-1}/\mathrm{N}$ for k_t and k_n respectively, whereas the theoretical values remained almost constant.
  These results show that using the available semi-analytical contact model to identify contact stiffness in an FE model is unsuccessful.
- The disagreement highlighted in the analysis can be partly explained by considering the meaning of the term "contact stiffness". In a numerical FE model, the contact stiffness represents the connection between two bodies through the nodes at the interfaces. The flexibility of the bulk, represented by the lobes on the root and the slot, is already considered in the finite element model. The semi-analytical model calculates the displacements and the stiffness, considering the elastic half-space. When theoretical stiffness is assembled in the FE model it is as if the bulk flexibility is considered twice.
- Moreover, when contact surfaces are loaded they deform because of the flexibility of the lobes. The pressure distribution becomes asymmetric, whereas the theoretical model assumes that the loads and the pressure distribution are symmetric. Since the contact problem is nonlinear, different pressure distributions result in different stiffness even if the total loads are the same. Currently, no theoretical models are available which consider the moment at the interface and asymmetric pressure distribution.

This work has shown that computing contact stiffnesses with a theoretical model, such as the one presented in the paper, and substituting them in a FE model underestimates the stiffness of the whole system. Designers should be aware that in this case the modal analysis and the forced response will be inaccurate. Quantifying this inaccuracy is a difficult task, as the results are highly dependent on the specific problem and its discretization. In the test case presented in this paper, the error on the frequency of the first and second mode ranged around 12 and 25%.

Table A.2
Measured natural frequencies uncertainties due to uncertainties on measured axial load F_{ax}.

F_{ax} kN	$\delta f^m_{n,1B}$ Hz	$\delta f^m_{n,2B}$ Hz
12	0.23	0.40
14	0.25	0.45
16	0.29	0.50
18	0.33	0.55
20	0.33	0.54
22	0.35	0.55

Declaration of competing interest

The authors declare that they have no known competing financial interests or personal relationships that could have appeared to influence the work reported in this paper.

Data availability

Data will be made available on request.

Appendix. Contact stiffness accuracy

Uncertainties on contact stiffness were estimated through the procedure shown in [57]. The numerical frequencies as a function of the contact stiffness can be approximated by a first order Taylor expansion

$$\mathbf{f}(k_n, k_t) = \left\{ \begin{array}{c} f^{FE}_{n,1B}(k_n, k_t) \\ f^{FE}_{n,2B}(k_n, k_t) \end{array} \right\} \simeq \mathbf{f_0} + \mathbf{J}\left(\mathbf{k} - \mathbf{k_0}\right) \tag{A.1}$$

with

$$\mathbf{k} = \left\{ \begin{array}{c} k_n \\ k_t \end{array} \right\} \tag{A.2}$$

and

$$\mathbf{J} = \left[\begin{array}{cc} \frac{\partial f_{n,1B}}{\partial k_n} & \frac{\partial f_{n,1B}}{\partial k_t} \\ \frac{\partial f_{n,2B}}{\partial k_n} & \frac{\partial f_{n,2B}}{\partial k_t} \end{array} \right] \tag{A.3}$$

Vector $\mathbf{k_0}$ contains a pair of trail solutions and $\mathbf{f_0}$ its corresponding frequencies. The uncertainties $\delta f_{n,1B}$ and $\delta f_{n,2B}$ on the frequencies for the first and second bending mode were obtained from the uncertainty on the measured axial load F_{ax} due to pressure gauge accuracy ($\delta p/p = \delta F_{ax}/F_{ax} = 1\%$).

$$\delta f_n = \frac{\partial f_n}{\partial F_{ax}} \delta F_{ax} \tag{A.4}$$

See Table A.2.

Sensitivity of the natural frequency f_n on axial load F_{ax} was estimated by using the FE model with the identified contact stiffnesses k_n and k_t. The frequency covariance matrix is

$$\boldsymbol{\sigma}^2 := \langle \delta\mathbf{f} \delta\mathbf{f}^T \rangle = \left[\begin{array}{cc} \sigma^2_{1B} & 0 \\ 0 & \sigma^2_{2B} \end{array} \right] = \left[\begin{array}{cc} \delta f^2_{n,1B} & 0 \\ 0 & \delta f^2_{n,2B} \end{array} \right] \tag{A.5}$$

with $\langle \cdot \rangle$ the expected value. In Eq. (A.5) the standard deviations σ_{1B} and σ_{2B} are approximated with the uncertainties $\delta f_{n,1B}$ and $\delta f_{n,2B}$. Thus, the covariance matrix of contact stiffness at $\mathbf{k_0}$ is

$$\sigma^2_{\mathbf{k}} = \left[\begin{array}{cc} \sigma^2_{nn} & \sigma^2_{nt} \\ \sigma^2_{tn} & \sigma^2_{tt} \end{array} \right] = \langle \delta\mathbf{k} \delta\mathbf{k}^T \rangle = \mathbf{J}^{-1} \langle \delta\mathbf{f} \delta\mathbf{f}^T \rangle (\mathbf{J}^{-1})^T = \mathbf{J}^{-1} \boldsymbol{\sigma}^2 (\mathbf{J}^{-1})^T \tag{A.6}$$

with $\delta\mathbf{f} = \mathbf{J}\delta\mathbf{k}$. The solution (named as optimal stiffness pair) was selected as the stiffness pair – on the minima locus – with the minimum 2-norm of the stiffness covariance matrix. Standard deviations of k_n and k_t were computed from the covariance matrix

$$\mathbf{k}^{opt} = \left\{ \begin{array}{c} k^{opt}_n \\ k^{opt}_t \end{array} \right\} : \qquad \min \|\sigma^2_{\mathbf{k}}\|_2 \quad \Rightarrow \quad \left\{ \begin{array}{l} k_n = k^{opt}_n \pm \sigma_{nn} \\ k_t = k^{opt}_t \pm \sigma_{tt} \end{array} \right. \tag{A.7}$$

References

[1] M. Lavella, D. Botto, Fretting fatigue analysis of additively manufactured blade root made of intermetallic Ti-48Al-2Cr-2Nb alloy at high temperature, Materials 11 (7) (2018) 1052, http://dx.doi.org/10.3390/ma11071052.

[2] M. Lavella, D. Botto, Fretting wear of alloy steels at the blade tip of steam turbines, Wear 426–427 (2019) 735–740, http://dx.doi.org/10.1016/j.wear.2019.01.039.

[3] D. Botto, A. Campagna, M. Lavella, M.M. Gola, Experimental and numerical investigation of fretting wear at high temperature for aeronautical alloys, in: Volume 6: Structures and Dynamics, Parts A and B, 2010, http://dx.doi.org/10.1115/gt2010-23356.

[4] M. Nakhla, J. Vlach, A piecewise harmonic balance technique for determination of periodic response of nonlinear systems, IEEE Trans. Circuits Syst. 23 (2) (1976) 85–91, http://dx.doi.org/10.1109/tcs.1976.1084181.

[5] K. Sanliturk, D. Ewins, Modelling two-dimensional friction contact and its application using harmonic balance method, J. Sound Vibr. 193 (2) (1996) 511–523, http://dx.doi.org/10.1006/jsvi.1996.0299.

[6] C. Pierre, A.A. Ferri, E.H. Dowell, Multi-harmonic analysis of dry friction damped systems using an incremental harmonic balance method, J. Appl. Mech. 52 (4) (1985) 958–964, http://dx.doi.org/10.1115/1.3169175.

[7] A. Cardona, A. Lerusse, M. Géradin, Fast Fourier nonlinear vibration analysis, Comput. Mech. 22 (2) (1998) 128–142, http://dx.doi.org/10.1007/s004660050347.

[8] C. Siewert, L. Panning, J. Wallaschek, C. Richter, Multiharmonic forced response analysis of a turbine blading coupled by nonlinear contact forces, Trans. ASME, J. Eng. Gas. Turbines Power 132 (8) (2010) http://dx.doi.org/10.1115/1.4000266.

[9] E.P. Petrov, D.J. Ewins, Analytical formulation of friction interface elements for analysis of nonlinear multi-harmonic vibrations of bladed disks, Trans. ASME, J. Turbomach. 125 (2) (2003) 364–371, http://dx.doi.org/10.1115/1.1539868.

[10] S. Zucca, C.M. Firrone, M.M. Gola, Numerical assessment of friction damping at turbine blade root joints by simultaneous calculation of the static and dynamic contact loads, Nonlinear Dynam. 67 (3) (2011) 1943–1955, http://dx.doi.org/10.1007/s11071-011-0119-y.

[11] S. Zucca, C.M. Firrone, Nonlinear dynamics of mechanical systems with friction contacts: Coupled static and dynamic multi-harmonic balance method and multiple solutions, J. Sound Vibr. 333 (3) (2014) 916–926, http://dx.doi.org/10.1016/j.jsv.2013.09.032.

[12] C. Gastaldi, T. Berruti, Competitive time marching solution methods for systems with friction-induced nonlinearities, Appl. Sci. 8 (2) (2018) 291, http://dx.doi.org/10.3390/app8020291.

[13] J. Griffin, Friction damping of resonant stresses in gas turbine engine airfoils, Trans. ASME, J. Eng. Gas. Turbines Power 102 (2) (1980) 329–333, http://dx.doi.org/10.1115/1.3230256.

[14] C. Menq, B. Yang, Non-linear spring resistance and friction damping of frictional constraint having two-dimensional motion, J. Sound Vibr. 217 (1) (1998) 127–143, http://dx.doi.org/10.1006/jsvi.1998.1739.

[15] B. Yang, C. Menq, Characterization of 3D contact kinematics and prediction of resonant response of structures having 3D frictional constraint, J. Sound Vibr. 217 (5) (1998) 909–925, http://dx.doi.org/10.1006/jsvi.1998.1802.

[16] B. Yang, M. Chu, C. Menq, Stick-slip-separation analysis and non-linear stiffness and damping characterization of friction contacts having variable normal load, J. Sound Vibr. 210 (4) (1998) 461–481, http://dx.doi.org/10.1006/jsvi.1997.1305.

[17] K.L. Johnson, Surface interaction between elastically loaded bodies under tangential forces, Proc. R. Soc. Lond. Ser. A Math. Phys. Eng. Sci. 230 (1183) (1955) 531–548, http://dx.doi.org/10.1098/rspa.1955.0149.

[18] B.N. Norden, On the Compression of a Cylinder in Contact with a Plane Surface, Technical Report, National Bureau of Standards, 1973, http://dx.doi.org/10.6028/nbs.ir.73-243.

[19] R. Roark, Formulas for Stress and Strain, McGraw-Hill, New York, 1975.

[20] J. Brandlein, P. Eschmann, L. Hasbargen, K. Weigand, Ball roller bearings, third ed., John Wiley & Sons, 1999.

[21] O. Kosarev, Contact deformation and compression of cylinders, Russ. Eng. Res. 31 (2) (2011) 107–112, http://dx.doi.org/10.3103/s1068798x11020122.

[22] C. Cattaneo, Sul contatto di due corpi elastici, Accad. Lincei, Rend. 6 (27) (1938) 342–348, 434–436, 474–478.

[23] R. Mindlin, Compliance of elastic bodies in contact, J. Appl. Mech. 16 (1949) 259–268.

[24] H. Deresiewicz, Oblique contact of nonspherical elastic bodies, J. Appl. Mech. 24 (4) (1957) 623–624.

[25] I. Shtayerman, Contact Problem of the Theory of Elasticity, Translation Division, Foreign Technology Division, 1970.

[26] M. Ciavarella, D.A. Hills, G. Monno, The influence of rounded edges on indentation by a flat punch, Proc. Inst. Mech. Eng. C 212 (4) (1998) 319–327, http://dx.doi.org/10.1243/0954406981521259.

[27] M. Allara, A model for the characterization of friction contacts in turbine blades, J. Sound Vibr. 320 (3) (2009) 527–544, http://dx.doi.org/10.1016/j.jsv.2008.08.016.

[28] M. Umer, D. Botto, Measurement of contact parameters on under-platform dampers coupled with blade dynamics, Int. J. Mech. Sci. 159 (2019) 450–458, http://dx.doi.org/10.1016/j.ijmecsci.2019.06.010.

[29] J. Chen, C. Zang, B. Zhou, E. Petrov, High-fidelity calculation of modal damping caused by friction at blade roots for single blades and tuned bladed disc assemblies, Proc. Inst. Mech. Eng. C (2020) 095440622093514, http://dx.doi.org/10.1177/0954406220935144.

[30] J. Chen, C. Zang, B. Zhou, E.P. Petrov, Analysis of nonlinear modal damping due to friction at blade roots in mistuned bladed disks, Trans. ASME, J. Eng. Gas Turbines Power 143 (3) (2021) http://dx.doi.org/10.1115/1.4049860.

[31] R.D. Mindlin, W.P. Mason, T.F. Osmert, H. Deresiewicz, Effects of an oscillating tangential force on the contact surfaces of elastic spheres, in: Proc. 1st Nat. Congr. Appl. Mech., 1952, pp. 203–208.

[32] L.E. Goodman, C.B. Brown, Energy dissipation in contact friction: Constant normal and cyclic tangential loading, J. Appl. Mech. 29 (1) (1962) 17–22, http://dx.doi.org/10.1115/1.3636453.

[33] S. Filippi, A. Akay, M.M. Gola, Measurement of tangential contact hysteresis during microslip, Trans. ASME, J. Tribol. 126 (3) (2004) 482–489, http://dx.doi.org/10.1115/1.1692030.

[34] S. Filippi, E.B. Rodrigues, M.M. Gola, Experimental characterization of contact hysteresis at high temperatures, in: Volume 5: Marine; Microturbines and Small Turbomachinery; Oil and Gas Applications; Structures and Dynamics, Parts A and B, in: Turbo Expo: Power for Land, Sea, and Air, 2006, pp. 893–902, http://dx.doi.org/10.1115/gt2006-90757.

[35] D. Botto, M. Lavella, High temperature tribological study of cobalt-based coatings reinforced with different percentages of alumina, Wear 318 (1–2) (2014) 89–97, http://dx.doi.org/10.1016/j.wear.2014.06.024.

[36] A.B. Stanbridge, D.J. Ewins, K.Y. Sanliturk, J.V. Ferreira, Experimental investigation of dry friction damping and cubic stiffness non-linearity, in: Volume 6B: 18th Biennial Conference on Mechanical Vibration and Noise, in: International Design Engineering Technical Conferences and Computers and Information in Engineering Conference, 2001, pp. 2141–2148, http://dx.doi.org/10.1115/detc2001/vib-21556.

[37] C. Schwingshackl, E. Petrov, D. Ewins, Measured and estimated friction interface parameters in a nonlinear dynamic analysis, Mech. Syst. Signal Proc. 28 (2012) 574–584, http://dx.doi.org/10.1016/j.ymssp.2011.10.005.

[38] M. Lavella, D. Botto, M.M. Gola, Test rig for wear and contact parameters extraction for flat-on-flat contact surfaces, in: ASME/STLE 2011 Joint Tribology Conference, in: International Joint Tribology Conference, 2011, pp. 307–309, http://dx.doi.org/10.1115/ijtc2011-61234.

[39] D. Li, D. Botto, C. Xu, M. Gola, A new approach for the determination of the iwan density function in modeling friction contact, Int. J. Mech. Sci. 180 (2020) 105671, http://dx.doi.org/10.1016/j.ijmecsci.2020.105671.
[40] D. Li, D. Botto, C. Xu, T. Liu, M. Gola, A micro-slip friction modeling approach and its application in underplatform damper kinematics, Int. J. Mech. Sci. 161–162 (2019) 105029, http://dx.doi.org/10.1016/j.ijmecsci.2019.105029.
[41] D. Li, C. Xu, D. Botto, Z. Zhang, M. Gola, A fretting test apparatus for measuring friction hysteresis of bolted joints, Tribol. Int. 151 (2020) 106431, http://dx.doi.org/10.1016/j.triboint.2020.106431.
[42] M. Umer, C. Gastaldi, D. Botto, Friction damping and forced-response of vibrating structures: An insight into model validation, Int. J. Solids Struct. 202 (2020) 521–531, http://dx.doi.org/10.1016/j.ijsolstr.2020.07.002.
[43] M. Allara, S. Filippi, M.M. Gola, An experimental method for the measurement of blade-root damping, in: Turbo Expo: Power for Land, Sea, and Air, Volume 5: Marine; Microturbines and Small Turbomachinery; Oil and Gas Applications; Structures and Dynamics, Parts A and B, 2006, pp. 903–912, http://dx.doi.org/10.1115/gt2006-90774.
[44] D. Botto, F. Cuccovillo, V. Iannotti, Experimental investigation of friction damping in blade root joints, J. Eng. Gas Turbines Power 145 (5) (2022) http://dx.doi.org/10.1115/1.4056099.
[45] C.M. Firrone, I. Bertino, Experimental investigation on the damping effectiveness of blade root joints, Exp. Mech. 55 (5) (2015) 981–988, http://dx.doi.org/10.1007/s11340-015-0001-9.
[46] F.J. Marquina, A. Coro, A. Gutiérrez, R. Alonso, D.J. Ewins, G. Girini, Friction damping modeling in high Stress Contact Areas using microslip friction model, in: Volume 5: Structures and Dynamics, Parts A and B, in: Turbo Expo: Power for Land, Sea, and Air, 2008, pp. 309–318, http://dx.doi.org/10.1115/gt2008-50359.
[47] K. Asai, S. Sakurai, T. Kudo, N. Ozawa, T. Ikeda, Evaluation of friction damping in dovetail root joints based on dissipation energy on contact surfaces, in: Volume 6: Structures and Dynamics, Parts A and B, in: Turbo Expo: Power for Land, Sea, and Air, 2009, http://dx.doi.org/10.1115/gt2009-59508.
[48] H.R. Simmons, V. Iyengar, Effect of non-uniform blade root friction and sticking on disk stresses, in: Volume 6: Structures and Dynamics, Parts A and B, in: Turbo Expo: Power for Land, Sea, and Air, 2011, pp. 829–838, http://dx.doi.org/10.1115/gt2011-46689.
[49] M. Feldman, Non-linear system vibration analysis using Hilbert transform–I. Free vibration analysis method 'Freevib', Mech. Syst. Signal Proc. 8 (2) (1994) 119–127, http://dx.doi.org/10.1006/mssp.1994.1011.
[50] M. Feldman, Hilbert Transform Applications in Mechanical Vibration, John Wiley & Sons, Ltd, 2011, http://dx.doi.org/10.1002/9781119991656.
[51] R.E. Ziemer, W.H. Tranter, Principles of Communication. Systems, Modulation, and Noise, seventh ed., John Wiley & Sons, 2014.
[52] A. Bokaian, Natural frequencies of beams under tensile axial loads, J. Sound Vibr. 142 (3) (1990) 481–498, http://dx.doi.org/10.1016/0022-460x(90)90663-k.
[53] R.R. Craig, M.C.C. Bampton, Coupling of substructures for dynamic analyses, AIAA J. 6 (7) (1968) 1313–1319, http://dx.doi.org/10.2514/3.4741.
[54] A.E.H. Love, A Treatise on the Mathematical Theory of Elasticity, Cambridge University Press, 1892.
[55] G. Starzynski, R. Buczkowski, Ultrasonic measurements of contact stiffness between rough surfaces, Trans. ASME, J. Tribol. 136 (3) (2014) http://dx.doi.org/10.1115/1.4027132.
[56] H. Andresen, D. Hills, J. Barber, J. Vázquez, Steady state cyclic behaviour of a half-plane contact in partial slip subject to varying normal load, moment, shear load, and moderate differential bulk tension, Int. J. Solids Struct. 182–183 (2020) 156–161, http://dx.doi.org/10.1016/j.ijsolstr.2019.07.027.
[57] P. Richter, Estimating Errors in Least-Squares Fitting, Techreport 42–122, NASA, 1995.